



Comparison and combination of rotational imaging optical coherence tomography and selective plane illumination microscopy for embryonic study

CHEN WU,¹ HENRY LE,² SHIHAO RAN,³ MANMOHAN SINGH,¹ IRINA V. LARINA,² DAVID MAYERICH,³ MARY E. DICKINSON,^{2,5,6} AND KIRILL V. LARIN^{1,2,4,5,7}

¹Department of Biomedical Engineering, University of Houston, Houston, TX 77204, USA

²Molecular Physiology and Biophysics, Baylor College of Medicine, Houston, TX 77584, USA

³Department of Electrical and Computer Engineering, University of Houston, Houston, TX 77204, USA

⁴Interdisciplinary Laboratory of Biophotonics, Tomsk State University, Tomsk 634050, Russia

⁵Equal contribution

⁶mdickins@bcm.edu

⁷klarin@central.uh.edu

Abstract: Several optical imaging techniques have been applied for high-resolution embryonic imaging using different contrast mechanisms, each with their own benefits and limitations. In this study, we imaged the same E9.5 mouse embryo with rotational imaging optical coherence tomography (RI-OCT) and selective plane illumination microscopy (SPIM). RI-OCT overcomes optical penetration limits of traditional OCT imaging that prohibit full-body imaging of mouse embryos at later stages by imaging the samples from multiple angles. SPIM enables high-resolution, 3D imaging with less phototoxicity and photobleaching than laser scanning confocal microscopy (LSCM) by illuminating the sample with a focused sheet of light. Side by side comparisons are supplemented with co-registered images. The results demonstrate that SPIM and RI-OCT are highly complementary and could provide more comprehensive tissue characterization for mouse embryonic research.

© 2017 Optical Society of America

OCIS codes: (110.4500) Optical coherence tomography; (170.2520) Fluorescence microscopy.

References and links

1. N. E. Sharpless and R. A. Depinho, "The mighty mouse: genetically engineered mouse models in cancer drug development," *Nat. Rev. Drug Discov.* **5**(9), 741–754 (2006).
2. S. R. Montezuma, D. Vavvas, and J. W. Miller, "Review of the ocular angiogenesis animal models," *Semin. Ophthalmol.* **24**(2), 52–61 (2009).
3. C. Biben, R. Weber, S. Kesteven, E. Stanley, L. McDonald, D. A. Elliott, L. Barnett, F. Köentgen, L. Robb, M. Feneley, and R. P. Harvey, "Cardiac septal and valvular dysmorphogenesis in mice heterozygous for mutations in the homeobox gene *Nkx2-5*," *Circ. Res.* **87**(10), 888–895 (2000).
4. B. G. Bruneau, G. Nemer, J. P. Schmitt, F. Charron, L. Robitaille, S. Caron, D. A. Conner, M. Gessler, M. Nemer, C. E. Seidman, and J. G. Seidman, "A murine model of Holt-Oram syndrome defines roles of the T-box transcription factor *Tbx5* in cardiogenesis and disease," *Cell* **106**(6), 709–721 (2001).
5. A. Greco, M. Mancini, S. Gargiulo, M. Gramanzini, P. P. Claudio, A. Brunetti, and M. Salvatore, "Ultrasound Biomicroscopy in Small Animal Research: Applications in Molecular and Preclinical Imaging," *J. Biomed. Biotechnol.* **2012**, 519238 (2012).
6. D. P. Clark and C. T. Badea, "Micro-CT of rodents: state-of-the-art and future perspectives," *Phys. Med.* **30**(6), 619–634 (2014).
7. B. J. Nieman and D. H. Turnbull, "Ultrasound and Magnetic Resonance Microimaging of Mouse Development," *Methods Enzymol.* **476**, 379–400 (2010).
8. M. E. Dickinson, "Multimodal imaging of mouse development: tools for the postgenomic era," *Dev. Dyn.* **235**(9), 2386–2400 (2006).
9. D. Huang, E. A. Swanson, C. P. Lin, J. S. Schuman, W. G. Stinson, W. Chang, M. R. Hee, T. Flotte, K. Gregory, C. A. Puliafito, and et, "Optical coherence tomography," *Science* **254**(5035), 1178–1181 (1991).

10. J. Fujimoto and E. Swanson, "The Development, Commercialization, and Impact of Optical Coherence Tomography," *Invest. Ophthalmol. Vis. Sci.* **57**(9), 1–13 (2016).
11. R. Raghunathan, M. Singh, M. E. Dickinson, and K. V. Larin, "Optical coherence tomography for embryonic imaging: a review," *J. Biomed. Opt.* **21**(5), 050902 (2016).
12. C. Wu, N. Sudheendran, M. Singh, I. V. Larina, M. E. Dickinson, and K. V. Larin, "Rotational imaging optical coherence tomography for full-body mouse embryonic imaging," *J. Biomed. Opt.* **21**(2), 026002 (2016).
13. J. Huisken, J. Swoger, F. Del Bene, J. Wittbrodt, and E. H. Stelzer, "Optical sectioning deep inside live embryos by selective plane illumination microscopy," *Science* **305**(5686), 1007–1009 (2004).
14. P. J. Keller and E. H. Stelzer, "Quantitative in vivo imaging of entire embryos with Digital Scanned Laser Light Sheet Fluorescence Microscopy," *Curr. Opin. Neurobiol.* **18**(6), 624–632 (2008).
15. J. Huisken and D. Y. Stainier, "Selective plane illumination microscopy techniques in developmental biology," *Development* **136**(12), 1963–1975 (2009).
16. R. K. Ejsmont, M. Sarov, S. Winkler, K. A. Lipinski, and P. Tomancak, "A toolkit for high-throughput, cross-species gene engineering in *Drosophila*," *Nat. Methods* **6**(6), 435–437 (2009).
17. P. J. Keller, A. D. Schmidt, J. Wittbrodt, and E. H. Stelzer, "Reconstruction of zebrafish early embryonic development by scanned light sheet microscopy," *Science* **322**(5904), 1065–1069 (2008).
18. H. U. Dodt, U. Leischner, A. Schierloh, N. Jähring, C. P. Mauch, K. Deininger, J. M. Deussing, M. Eder, W. Zieglgänsberger, and K. Becker, "Ultramicroscopy: three-dimensional visualization of neuronal networks in the whole mouse brain," *Nat. Methods* **4**(4), 331–336 (2007).
19. M. W. Jenkins, M. Watanabe, and A. M. Rollins, "Longitudinal Imaging of Heart Development With Optical Coherence Tomography," *IEEE J. Sel. Top. Quantum Electron.* **18**(3), 1166–1175 (2012).
20. B. A. Filas, I. R. Efimov, and L. A. Taber, "Optical coherence tomography as a tool for measuring morphogenetic deformation of the looping heart," *Anat. Rec. (Hoboken)* **290**(9), 1057–1068 (2007).
21. S. Wang, M. D. Garcia, A. L. Lopez, P. A. Overbeek, K. V. Larin, and I. V. Larina, "Dynamic imaging and quantitative analysis of cranial neural tube closure in the mouse embryo using optical coherence tomography," *Biomed. Opt. Express* **8**(1), 407–419 (2017).
22. S. H. Syed, K. V. Larin, M. E. Dickinson, and I. V. Larina, "Optical coherence tomography for high-resolution imaging of mouse development in utero," *J. Biomed. Opt.* **16**(4), 046004 (2011).
23. J. Men, Y. Huang, J. Solanki, X. Zeng, A. Alex, J. Jerwick, Z. Zhang, R. E. Tanzi, A. Li, and C. Zhou, "Optical Coherence Tomography for Brain Imaging and Developmental Biology," *IEEE J. Sel. Top. Quantum Electron.* **22**(4), 6803213 (2016).
24. J. L. Lucitti, E. A. V. Jones, C. Huang, J. Chen, S. E. Fraser, and M. E. Dickinson, "Vascular remodeling of the mouse yolk sac requires hemodynamic force," *Development* **134**(18), 3317–3326 (2007).
25. D. Zhu, K. V. Larin, Q. Luo, and V. V. Tuchin, "Recent progress in tissue optical clearing," *Laser Photonics Rev.* **7**(5), 732–757 (2013).
26. M. Mickoleit, B. Schmid, M. Weber, F. O. Fahrbach, S. Hombach, S. Reischauer, and J. Huisken, "High-resolution reconstruction of the beating zebrafish heart," *Nat. Methods* **11**(9), 919–922 (2014).
27. J. Icha, C. Schmied, J. Sidhaye, P. Tomancak, S. Preibisch, and C. Norden, "Using Light Sheet Fluorescence Microscopy to Image Zebrafish Eye Development," *J. Vis. Exp.* **110**, e53966 (2016).
28. J. R. Walls, L. Coultas, J. Rossant, and R. M. Henkelman, "Three-dimensional analysis of vascular development in the mouse embryo," *PLoS One* **3**(8), e2853 (2008).
29. N. Sudheendran, S. Syed, M. Dickinson, I. Larina, and K. Larin, "Speckle variance OCT imaging of the vasculature in live mammalian embryos," *Laser Phys. Lett.* **8**(3), 247–252 (2011).
30. G. Liu, W. Qi, L. Yu, and Z. Chen, "Real-time bulk-motion-correction free Doppler variance optical coherence tomography for choroidal capillary vasculature imaging," *Opt. Express* **19**(4), 3657–3666 (2011).
31. R. K. Wang and L. An, "Doppler optical micro-angiography for volumetric imaging of vascular perfusion in vivo," *Opt. Express* **17**(11), 8926–8940 (2009).
32. S. Wang, M. Singh, A. L. Lopez, C. Wu, R. Raghunathan, A. Schill, J. Li, K. V. Larin, and I. V. Larina, "Direct four-dimensional structural and functional imaging of cardiovascular dynamics in mouse embryos with 1.5 MHz optical coherence tomography," *Opt. Lett.* **40**(20), 4791–4794 (2015).
33. I. V. Larina, S. Ivers, S. Syed, M. E. Dickinson, and K. V. Larin, "Hemodynamic measurements from individual blood cells in early mammalian embryos with Doppler swept source OCT," *Opt. Lett.* **34**(7), 986–988 (2009).
34. R. S. Udan, V. G. Piazza, C. W. Hsu, A. K. Hadjantonakis, and M. E. Dickinson, "Quantitative imaging of cell dynamics in mouse embryos using light-sheet microscopy," *Development* **141**(22), 4406–4414 (2014).
35. Y. N. Tallini, B. Shui, K. S. Greene, K. Y. Deng, R. Doran, P. J. Fisher, W. Zipfel, and M. I. Kotlikoff, "BAC transgenic mice express enhanced green fluorescent protein in central and peripheral cholinergic neurons," *Physiol. Genomics* **27**(3), 391–397 (2006).
36. Y. S. Huang, H. Y. Ku, Y. C. Tsai, C. H. Chang, S. H. Pao, Y. H. Sun, and A. Chiou, "5D imaging via light sheet microscopy reveals cell dynamics during the eye-antenna disc primordium formation in *Drosophila*," *Sci. Rep.* **7**, 44945 (2017).
37. T. V. Truong, W. Supatto, D. S. Koos, J. M. Choi, and S. E. Fraser, "Deep and fast live imaging with two-photon scanned light-sheet microscopy," *Nat. Methods* **8**(9), 757–760 (2011).
38. T. Vetterburg, H. I. Dalgarno, J. Nytk, C. Coll-Lladó, D. E. Ferrier, T. Čizmar, F. J. Gunn-Moore, and K. Dholakia, "Light-sheet microscopy using an Airy beam," *Nat. Methods* **11**(5), 541–544 (2014).

39. M. Singh, R. Raghunathan, V. Piazza, A. M. Davis-Loiacono, A. Cable, T. J. Vedakkan, T. Janacek, M. V. Frazier, A. Nair, C. Wu, I. V. Larina, M. E. Dickinson, and K. V. Larin, "Applicability, usability, and limitations of murine embryonic imaging with optical coherence tomography and optical projection tomography," *Biomed. Opt. Express* **7**(6), 2295–2310 (2016).
40. A. Bassi, B. Schmid, and J. Huisken, "Optical tomography complements light sheet microscopy for in toto imaging of zebrafish development," *Development* **142**(5), 1016–1020 (2015).
41. J. Mayer, A. Robert-Moreno, R. Danuser, J. V. Stein, J. Sharpe, and J. Swoger, "OPTiSPIM: integrating optical projection tomography in light sheet microscopy extends specimen characterization to nonfluorescent contrasts," *Opt. Lett.* **39**(4), 1053–1056 (2014).
42. J. F. Colas and J. Sharpe, "Live optical projection tomography," *Organogenesis* **5**(4), 211–216 (2009).

1. Introduction

The mouse is the most common model of mammalian development due to its biological similarity to humans and accessibility to numerous genetically engineered mouse (GEM) models for simulating human pathologies [1, 2]. For instance, mouse embryonic research has provided insight into the genetic and developmental etiology of congenital heart diseases [3, 4]. To better characterize the morphological alteration of embryonic structures, a wide range of imaging techniques are available to study mouse embryonic development, including ultrasound biomicroscopy (UBM), micro computed tomography (micro-CT), and micro magnetic resonance imaging (micro-MRI). Each method provides different advantages based on their underlying physical principles. UBM can achieve a typical spatial resolution of ~50 μm using high frequency ultrasound (40-100 MHz), which is sufficient to observe gross anatomical details [5]. Typical resolutions achievable by micro-CT are on the order of 100 μm , in live tissues; however, micro-CT has low intrinsic contrast in soft tissues. Consequently, a relatively high radiation dose is necessary to achieve a sufficient signal-to-noise ratio and tissue fixation is required for the highest resolution and signal-to-noise to be achieved [6]. Micro-MRI provides high contrast and relatively high resolution (<100 μm), but requires long acquisition times and is therefore unsuitable for real time imaging [7]. Optical imaging modalities, such as confocal and multiphoton microscopy, provide the best compromise of speed, resolution, and penetration depth at the scales necessary for dynamic murine embryo imaging at cellular or sub-cellular resolution. Unfortunately, there is no single technique that is capable of noninvasive, *in vivo*, whole-body imaging at subcellular resolution with the ability to produce contrast from any structure of interest [8]. However, complementary imaging techniques could be combined to provide additional information inaccessible using a single method.

Optical coherence tomography (OCT) is a well-established imaging technique with micrometer scale spatial resolution [9]. OCT was initially developed for applications in ophthalmology [10], but has proven to be a powerful method for embryonic research [11]. It is able to perform cross-sectional imaging by detecting backscattered light from samples utilizing the principle of low coherence interferometry [9]. OCT is capable of noninvasive, real-time, 3D imaging of tissue microstructure with micrometer-scale spatial resolution and a penetration depth of ~1 to ~2 mm within highly scattering tissues. Because conventional OCT suffers from limited imaging depth in scattering media, we have developed rotational imaging OCT (RI-OCT) to increase the imaging depth. RI-OCT obtains structural information at four orthogonal angles, which are then co-registered to form a single three-dimensional image. The enhanced depth allows imaging of deeper structures, which is particularly beneficial for later stage murine embryos [12].

In contrast to OCT, fluorescence imaging provides biochemical, metabolic, and molecular information using fluorescent labels available through staining or using transgenic animals. Fluorescent imaging is in common use and several techniques offer microscopic resolutions and high throughput. Among them, selective plane illumination microscopy (SPIM) is a promising fluorescence microscopic technique for studying murine embryonic development [13]. SPIM, also called light sheet fluorescence microscopy or LSFM, uses a thin plane of light to optically section samples labeled with a fluorophore. This technique provides

comparable resolution to confocal microscopy at a much faster rate. SPIM is able to produce high-quality and high-resolution serial sections with minimal photo-bleaching and photo-toxicity [14], which makes SPIM a powerful technique for three-dimensional imaging [15].

With the aforementioned advantages, SPIM can image larger specimens, such as mouse embryos, with sufficient (micrometer scale) resolution for fine structures. Thus, SPIM is well suited for longitudinal imaging of developmental processes at multiple scales for investigating of early embryogenesis. Its applications include imaging molecular interactions and gene expression patterns [16], early developmental dynamics [17], and large fixed specimens *in toto* [18]. When imaging thick and highly scattering samples, SPIM still suffers from reduced lateral resolution. In contrast, OCT can capture morphological changes in deep structures due to its reliance on both infrared light and the high dynamic range afforded by coherence gating. In addition, the contrast in OCT images comes from the optical scattering properties of tissue, and thus OCT can capture valuable structural features by depicting tissue boundaries. For example, OCT has been frequently utilized to study embryonic heart morphogenesis during cardiac looping process to understand the etiology of congenital heart defects [19, 20]. Recently OCT was used to image the neural tube closure which is a critical process in the development of neural tube defects [21]. Quantitative assessment of different developmental processes, such as the formation of the brain and limb growth in normal and pathological states has also been performed [22, 23]. Given their different contrast mechanisms, the combination of OCT and SPIM can provide complementary information for a deeper understanding of embryogenesis.

In this study, we have explored the feasibility of combining images acquired separately with RI-OCT and SPIM from the same embryo. Preliminary testing was performed on microbeads embedded in phantoms. Mouse embryos 9.5 days post-coitum (E9.5) were then imaged by the two techniques and our results show great promise for multimodal imaging by SPIM and OCT. Another benefit for combining both RI-OCT and SPIM is that sample rotation could be performed so that each side of the sample is imaged with the highest contrast.

2. Materials and methods

2.1 OCT and SPIM imaging systems

A schematic of the RI-OCT setup is illustrated in Fig. 1(a). The RI-OCT setup was based on a commercial swept-source OCT (SS-OCT) system (OCS1310V2, Thorlabs, NJ, USA) with a central wavelength of ~ 1300 nm, bandwidth of ~ 100 nm, and scan rate of 200 kHz. A scan lens (LSM03, Thorlabs, NJ, USA) was used in this system with an effective focal length of 36 mm. The axial resolution of the SS-OCT system was measured at ~ 12 μ m, and the transverse resolution was about ~ 10 μ m, both in air. The imaging depth of the system was ~ 6 mm, with a ~ 120 μ m depth of focus. A square glass cuvette was mounted on a rotational stage to hold the sample. Conventional 3D OCT structural imaging was performed on the sample as the stage was rotated at four different angles with an interval of 90 degrees. The images were then co-registered after acquisition.

The SPIM system was slightly modified from a commercial system (Lightsheet Z.1, Carl Zeiss Microscopy, GmbH, Germany). The system splits fluorescence excitation and detection into two separate paths, with the detection axis perpendicular to the illumination axis. The sample was illuminated from both sides at 488 nm and 561 nm. The samples were imaged with a 5X air detection objective (Plan-Neofluar N.A. of 0.16), with 5X (N.A. of 0.1) illumination objective, respectively. The axial resolution (the thickness of the light sheet) was 5.2 μ m and lateral resolutions (across the light sheet) was 1.3 μ m respectively, at a magnification of 0.7 for the images taken with the 5X objective. The sample cuvette was placed inside a water filled chamber and positioned precisely in three dimensions with piezoelectric actuators. Half the sample was scanned through from one side with dual illumination, then the sample was rotated 180 degrees and imaged from the other side with

same settings. The dual illumination and imaging angles were fused after imaging using mean fusion method in Zen 2.1 lightsheet software, where the pixel in the fused image is determined by averaging the intensity level of the pixels for the involved views.

2.2 Phantoms

To investigate the feasibility of multimodal imaging with SPIM and OCT, a phantom was prepared using fluorescence microbeads (various sizes of 10-20 μm , 63-75 μm , 300-355 μm and 500-600 μm) distributed in 1% (w/w) agar. The agar was then poured into a cuvette and imaged after hardening using both techniques. Special care was taken to image the phantom at the same position and orientation to ensure precise image registration.

2.3 Animals

Mouse embryos (strain *Tg; ϵ -globin-GFP*) were imaged by both techniques. *Tg; ϵ -globin-GFP* is expressed in early erythroblast formation and previously used to study the role of hemodynamic forces during embryonic development [24]. Paired matings were set up overnight, and copulation was determined by the presence of a vaginal plug in the morning (thus embryos were marked as E0.5). Embryos were dissected out of the mothers at E9.5 (9.5 days post-coitum) and imaged with RI-OCT and SPIM. Embryos were fixed for 2h in 4% paraformaldehyde before being permeabilized in 1x PBS + 0.5% Triton X-100 (PBS-T). Non-specific antibody binding was blocked with 2% bovine goat serum in PBS-T for 2h at 4 °C. Embryos were incubated primary anti-PECAM1 antibody (1:200, Mec13.3, BD Pharmingen) diluted in blocking solution overnight at 4 °C. Primary antibody was counter stained with Alexa Fluor 568 goat anti-rat secondary antibody (1:500, Invitrogen, Corp), which was diluted in blocking solution for 1h at 4 °C. The embryos were first imaged by the RI-OCT method, and then imaged using SPIM.

2.4 Image process and registration

Image acquisition and processing procedures for RI-OCT have been detailed in our previous publication [12]. Briefly, RI-OCT acquires normal 3D OCT structural images at different angles by rotating the sample, which is mounted on a rotational stage. After rescaling the images to physical dimensions by correcting for refractive indices, the images were rotated and co-registered based on the rotation and translation of the sample. For SPIM imaging, the data sets acquired from both sides were initially aligned and combined with the instrument software (ZEN, Carl Zeiss Microscopy GmbH, Germany). Manual image co-registration and volumetric rendering of OCT and SPIM images were conducted in Amira (FEI Co., OR, USA) after rescaling the images to physical dimensions. Both data sets were imported into Amira, rescaled to proper physical dimensions by setting pixel sizes, and translated/rotated to achieve proper alignment. The transformation was edited interactively in the 3D viewer using the Open Inventor draggers in Amira. The transformation parameters were adjusted until the general contours overlapped. Finer alignment was performed by simultaneous visualization of cross sections from two data sets. For 3D rendering of matched volumes, the OCT data was assigned to the grey color channel, and the SPIM data was assigned to the red channel. The intensity and opacity of each individual color channel were adjusted for better visualization.

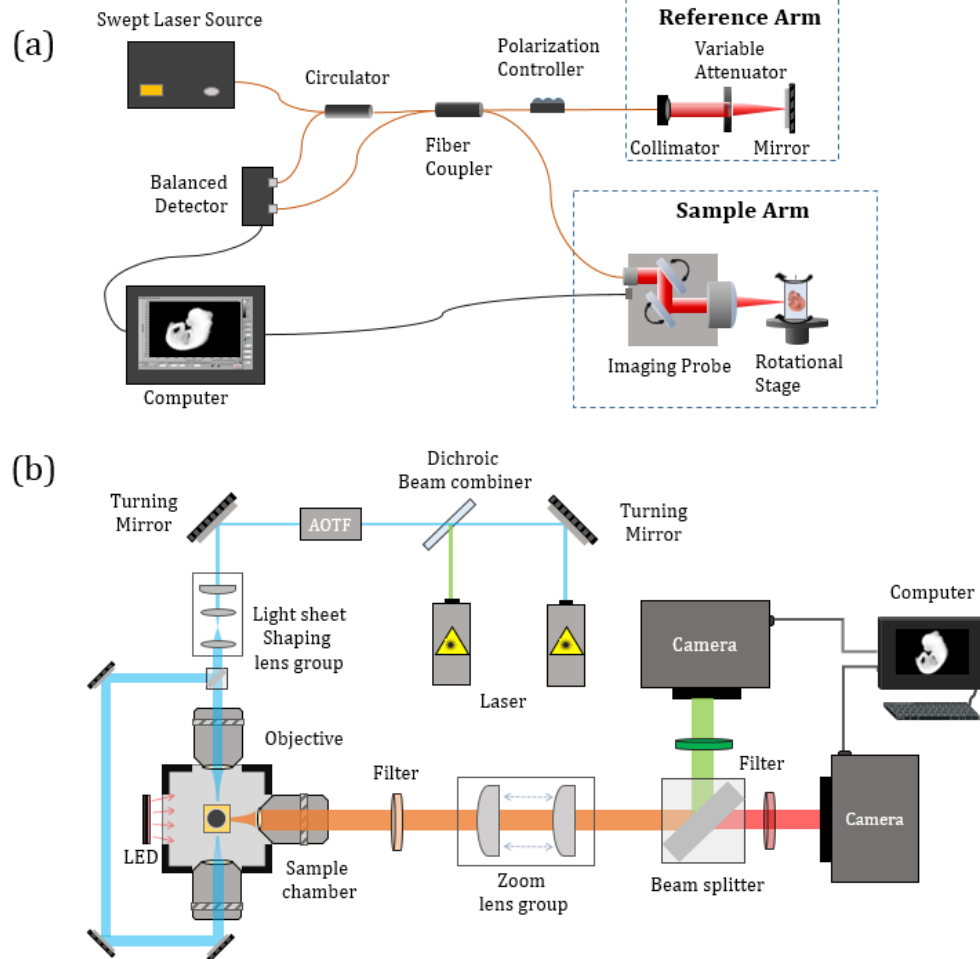


Fig. 1. Schematic of (a) RI-OCT experimental setup and (b) SPIM setup.

3. Results and discussion

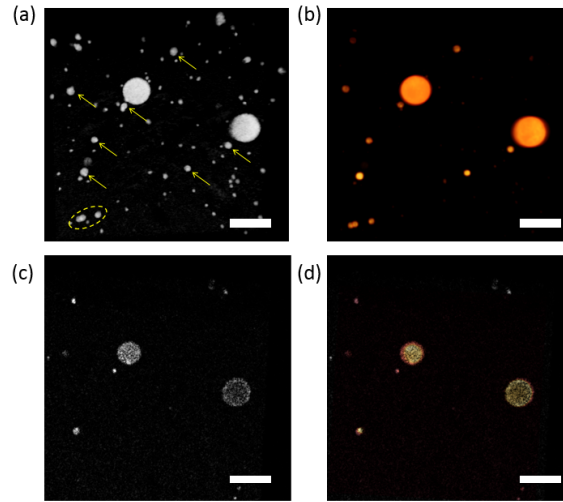


Fig. 2. (a) 3D OCT and (b) SPIM imaging of beads phantom. (c) Cross-sectional OCT image of selected plane. (d) Combined OCT and SPIM images of the same cross-sectional plane. Scale bars are 500 μm .

Figures 2(a) and 2(b) show 3D rendering of the bead phantoms imaged using OCT and SPIM (at an excitation wavelength of 488nm), respectively. Two large beads can be easily identified, and their relative positions in the image is the same in the OCT and SPIM images. Small microbeads (indicated by the yellow arrows and yellow dashed circles) are also located in the same relative positions in both images. Figure 2(c) is an OCT cross sectional image from a selected plane, and Fig. 2(d) is same OCT cross sectional image overlapped with the corresponding SPIM image, which indicates that the data from the two imaging modalities can be well co-registered.

Figures 3(a)-3(d) depict volumetric renderings of the RI-OCT of mouse embryo obtained from different angles, and Figs. 3(e)-3(h) are combined RI-OCT images from different views. Figures 3(i) and 3(j) present the SPIM images of the embryos from opposite sides, and Fig. 3(k) and 3(l) show the merged SPIM images.

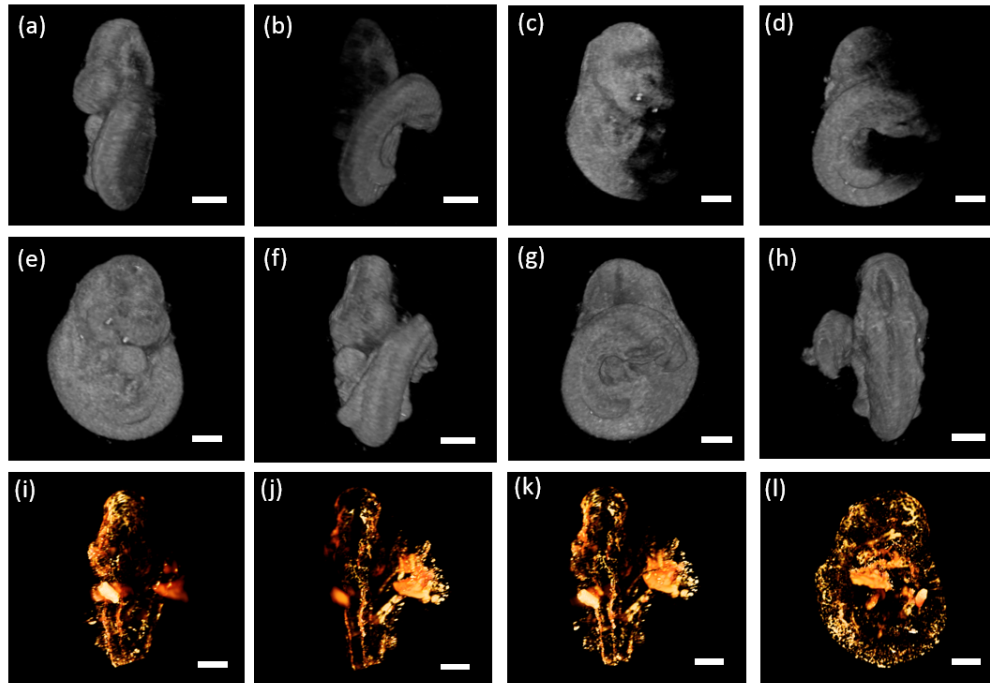


Fig. 3. RI-OCT imaging of E9.5 mouse embryo at (a) 0 degree, (b) 180 degree, (c) 90 degree, (d) 270 degree, (e-h) composite from all four angles. SPIM imaging of same embryo from (i) one side, (j) opposite side, and (k-l) combined from both sides. Scale bars are 500 μm .

The co-registered OCT and SPIM images of an E9.5 mouse embryo are shown in Fig. 4. Figure 4(a) presents a 3D RI-OCT rendering of the mouse embryo, Fig. 4(b) and 4(c) shows the 3D SPIM images of same embryo excited at 488nm and 561nm, respectively. Figure 4(d) presents the co-registered 3D OCT and SPIM images. Figures 4(e)-4(h) are co-registered images from selected 2D cross-sections. Endothelial cells labeled by PECAM1 show that the embryo vascular structure can be visualized in high detail with SPIM. The vasculature is widely distributed in the brain, spine, and tail of the embryo. Various embryonic structures could be identified, such as the dorsal aorta, neuro lumen, and intersomitic vessel. Combined with the ϵ -globin-GFP excited at 488 nm, it is possible to see how blood was distributed in different organs at the time of fixation. The brain had more erythrocytes trapped in the microvascular network, and many erythrocytes were also found in the heart, limb, and dorsal aorta. The PECAM1 signal is much stronger in and around the heart due to the presence of the rapidly developing cardiovascular system at this embryonic stage. From SPIM cross sectional images, it is possible to visualize the internal and external structure of the heart. GFP and PECAM1 labeled cells show the myocardium and erythrocytes, while OCT can reveal the heart wall thickness as indicated by the arrowhead in Fig. 4(e). However, the light was aberrated due to the embryo tissue, resulting in blurring that is visible in the images, particularly in the internal structures of the embryo. Clearing protocols can ameliorate this issue, but their toxicity is not suitable for live imaging [25]. Moreover, most SPIM publications focus on clear samples, such as zebrafish, which do not encounter such issues during imaging [26, 27].

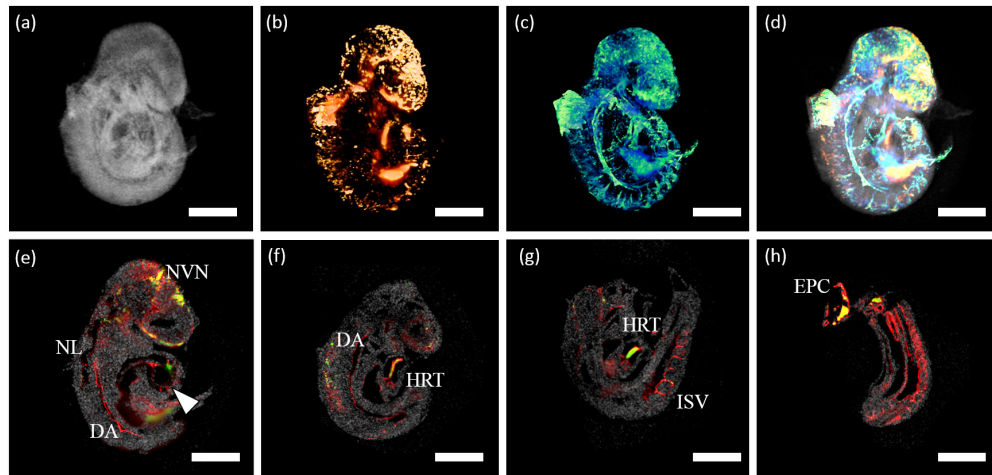


Fig. 4. E9.5 mouse embryo. (a) 3D OCT image. (b) 3D SPIM image at an excitation wavelength of 488nm corresponding to the ϵ -globin-GFP cells (erythroblast). (c) 3D SPIM image at an excitation wavelength of 561nm for PECAM1 labeled endothelial cells. (d) 3D registered OCT and SPIM image (see Visualization 1). (e-h) 2D OCT image registered with SPIM image for various planes, and arrowhead points to the heart wall. DA: dorsal aorta, HRT: heart, EPC: ectoplacental cone, NL: neuro lumen, NVN: neuro vascular network, ISV: intersomitic vessel.

4. Discussion

In this study, both the structure and the vasculature of an E9.5 mouse embryo were imaged. Major vasculogenesis and angiogenesis occur in the mouse embryo between E8.0 and E10.0, during which time the vasculature develops from a simple circulatory loop into a complex and fine structured system [28]. Therefore, E9.5 is a suitable stage to study vasculature development. As discussed previously, optical clearing is usually necessary for SPIM imaging for large and highly scattering tissues but is not suitable for *in vivo* applications. As shown in this study, tissue scattering is not completely prohibitive for SPIM imaging of E9.5 embryos, and RI-OCT enables whole-body imaging of E9.5 murine embryos. Thus, the combination of these techniques is suitable for embryos at this stage. However, imaging whole, unmodified embryos at later developmental stages is still a challenge for SPIM and RI-OCT.

Although OCT is also able to visualize blood vessels in biological tissue with various angiography techniques [29–31], it requires blood flow of a sufficient velocity to provide contrast between surrounding tissues. In this preliminary study, the embryo was fixed in agar, and thus was not suitable for angiographic imaging. The erythroblasts were labeled with GFP for fluorescence imaging by SPIM and OCT-based angiographic techniques may not be able to provide the spatial resolution of SPIM, with which each cell could be visualized and tracked. However, OCT-based angiography is label-free, and we have shown a technique capable of 3D video-rate volumetric speckle variance based angiography *in vivo* in cultured mouse embryos [32]. The high temporal resolution of OCT is well-suited for studying the dynamics in the embryo cardiovascular system, such as blood flow and heart function [33]. On the other hand, SPIM has the advantage of labeling multiple cell types of interest, which is useful for studying the dynamics of cell migration and cell proliferation during embryo development [34–36]. In SPIM, the imaging depth limits spatial resolution when imaging thicker samples, as the signal gets weaker and scatters when imaging deep within the tissue. Multiple methods have been developed to overcome depth limits, including double-sided illumination, multiview acquisition, and clearing. However, multiview acquisition increasing acquisition and processing time. Another method to improve the penetration depth of SPIM

imaging is to utilize two-photon excitation. Truong et al. have demonstrated that two-photon SPIM could achieve a penetration depth two times better than one-photon SPIM for imaging of fly embryos [37]. Clearing is not suitable for live imaging, can quench fluorescence signals, and only inorganic clearing solutions are compatible with the light sheet system. Also, there is a trade-off between high spatial resolution and field of view. In this study, we chose a large imaging field to capture the whole embryo at the cost of spatial resolution. A larger field of view could be accomplished at a higher resolution by performing mosaic imaging, but the trade-off would be an increase in the imaging and co-registration time. In contrast, the spatial resolution of OCT is defined in the axial direction by the bandwidth of the broadband source, and the transverse resolution and axial depth of field are defined by the NA of the objective or scan lens. However, multi-focus scanning techniques such as Gabor domain OCT or numerical re-focusing can overcome the limited depth of field from high NA applications. Another solution is the use of non-diffracting beams, such as Airy beams [38]. Nevertheless, for early stage embryos (e.g. E9.5), a depth of field of a few millimeters is sufficient for whole-body embryo imaging [12, 39].

In addition to OCT, optical projection tomography (OPT) is another powerful technique to study the embryo morphology. OPT and SPIM have been combined for complementary imaging of murine embryos and zebrafish [40, 41]. We have previously compared the performance of OCT and OPT for imaging murine embryos, where we observed similar results that OCT was unable to wholly image embryos beyond E9.5. OPT was able to image entire later stage embryos (up to E13.5) but requires a lengthy clearing and fixation procedure, while OCT can perform live imaging [39]. Although live OPT imaging of murine embryos has been demonstrated, only a limb bud was successfully imaged [42].

In this study, the mouse embryo was fixed in agar to avoid any movement while moving the sample between the two imaging systems. Embedding the sample in agar may be suitable for samples such as zebrafish, but it is not applicable for murine embryos due to their rapid growth and need for a controlled environment for *ex utero* culturing [34]. Our next step is to combine the systems into a single instrument with synchronized acquisition to eliminate the need for immobilizing the embryos and enable *in vivo* imaging. In the current work, a commercial SPIM system was utilized, which is not convenient for integrating OCT. This study has shown the feasibility of combining OCT and SPIM imaging of the same embryo for the first time and lays the foundation for the development of a dual-modality OCT/SPIM system. The same registration method could be directly applied to the dual modality system. Our future work will focus on developing a customized SPIM system, similar to the Open-SPIM, which will combine SPIM and OCT into a single multimodal embryonic imaging system. The main advantage of a dual modality instrument is the elimination of transferring the sample, ensuring that the embryo is imaged in the same conditions. Moreover, a dual modality setup would enable easier live imaging by imaging the embryo in a culture medium, which could provide a more robust growth environment. In addition, various parameters can be analyzed with SPIM imaging such as cell proliferation, cell death, cell type identification, and cell signaling, while OCT would provide complementary structural information. It will be more beneficial for mouse embryonic developmental study.

5. Conclusion

In this study, we compared and combined images of GFP-expressing mouse embryos obtained by RI-OCT and SPIM. Fluorescent microbeads and a E9.5 mouse embryo was imaged with both imaging techniques, and the images were co-registered. The results show that the images from both methods can be registered well after rescaling to physical dimensions. RI-OCT provided high-resolution whole-body structural imaging of an E9.5 mouse embryo, and SPIM imaged the embryo vasculature with high resolution as well. Our future work will be focused on integrating the two imaging systems into one dual-modality setup.

Funding

This work was supported, in part, by grants from the National Institute of Health R01HL120140 (IL), R01HD086765 (KL), R01HL128064 (MED), U54 HG006348-S1 (MED), UM1HG006348 (MED), R00LM011390-02 (DM), and CPRIT RR140013 (DM).